Inorganic Chemistry

Article

pubs.acs.org/IC

$Ba_4Ta_2O_9$ Oxide Prepared from an Oxalate-Based Molecular Precursor—Characterization and Properties

Lidija Androš,[†] Marijana Jurić,*[,†] Jasminka Popović,[†] Ana Šantić,[†] Predrag Lazić,[†] Metka Benčina,[‡] Matjaz Valant,[‡] Nevenka Brničević,[†] and Pavica Planinić[†]

[†]Ruđer Bošković Institute, Bijenička cesta 54, 10000 Zagreb, Croatia

[‡]Materials Research Laboratory, University of Nova Gorica, Vipavska 13, 5000 Nova Gorica, Slovenia

Supporting Information

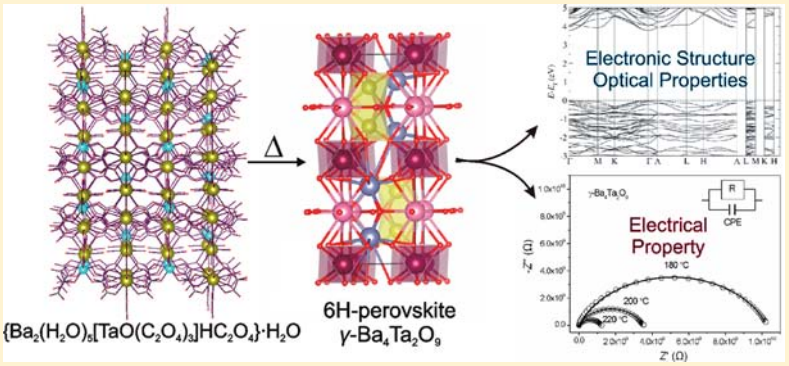

ABSTRACT: A novel heterometallic oxalate-based compound, $\{Ba_2(H_2O)_5[TaO(C_2O_4)_3]HC_2O_4\}\cdot H_2O$ (**1**), was obtained by using an (oxalato)tantalate(V) aqueous solution as a source of the complex anion and characterized by X-ray single-crystal diffraction, IR spectroscopy, and thermal analysis. Compound **1** is a three-dimensional (3D) coordination polymer with the Ta atom connected to eight neighboring Ba atoms through the oxalate ligands and the oxo oxygen group. Thermal treatment of **1** up to 1200 °C leads to molecular precursor-to-material conversion that yields the mixed-metal γ-$Ba_4Ta_2O_9$ phase. This high-temperature γ-$Ba_4Ta_2O_9$ polymorph has the *6H*-perovskite structure (space group $P6_3/m$), in which the Ta_2O_9 face-sharing octahedral dimers are interconnected via corners to the regular BaO_6 octahedra. To date, γ-$Ba_4Ta_2O_9$ has never been obtained at room temperature, because of the reduction of symmetry ($P6_3/m \rightarrow P2_1/c$) that usually occurs during the cooling. Spectroscopic, optical, photocatalytic, and electrical properties of the obtained γ-$Ba_4Ta_2O_9$ phase were investigated. In addition to the experimental data, an absorption spectrum and band structure of the γ-$Ba_4Ta_2O_9$ polymorph were calculated using density functional theory.

INTRODUCTION

Mixed-metal oxides are an important class of advanced materials, due to their wide range of technological applications. They are mostly utilized as catalysts and structural ceramics, but recently, the use of mixed-metal oxides as sensors, actuators, and smart materials has also been explored.[1]

So far, a large number of photocatalysts have been reported to effectively split water. However, most of these materials function as photocatalysts only under UV light irradiation because of their wider band gap of ~3.2−4 eV. Thus, in the past few years it has been a research challenge to develop photocatalyst materials that can utilize visible light. This implies that such materials should function in the visible light region ($420\ nm < \lambda < 800\ nm$) with a band gap of ideally about 2 eV.[2] Recent studies on some tantalates and niobates have revealed high photochemical and photocatalytic activities owing to their semiconducting nature.[2] The tantalates possess conduction bands consisting of Ta 5d orbitals located at a more negative energy (with respect to SHE) than titanates (Ti 3d) and niobates (Nb 4d).[3] Direct splitting of water under visible light irradiation has been detected in an oxide semiconductor photocatalyst: i.e., $InTaO_4$.[3] The tantalates are good photocatalysts not only for water splitting but also for degradation of environmental pollutants.[4] In addition, Ta-based materials such as $SrBi_2Ta_2O_9$ (SBT) and $LiTaO_3$ have attracted much attention in microelectronics and optoelectronics, in applications such as ferroelectric memories, light switches, and modulators.[5,6]

Alkoxides of tantalum are the most common precursors for the syntheses of Ta-based oxides using the sol−gel method. These precursors are expensive and sensitive to moisture, unlike $TaCl_5$. However, when using $TaCl_5$ a small concentration of residual chloride might cause deterioration of optoelectronic and dielectric properties of the final material.[7] On the other hand, air-stable, water-soluble tantalum

Received: September 7, 2013
Published: November 27, 2013

   dx.doi.org/10.1021/ic402276e | *Inorg. Chem.* 2013, 52, 14299−14308

precursors are still not easily available. Several research groups have made some progress in this area.[8−12] Thus, the Nelis[13−15] and Varela[16,17] groups systematically investigated the preparation and ferroelectric properties of the SBT films using a commercial Ta oxalate. The investigations of tantalum precursors with the use of cheap and stable Ta_2O_5 as a starting substance are thus far very scarce.[18] Due to the growing need for multicomponent oxide materials of tantalum(V), further investigation of the Ta-containing heterometallic compounds that could serve as single-source molecular precursors for the preparation of the Ta-based oxides is of great importance.

In general, a conventional way to prepare oxide materials is based on the solid-state reactions between the binary oxides. This method requires a heat treatment at relatively high temperatures, usually above 1000 °C, as well as long-term and repeated grinding procedures. Frequently, it yields low-purity products with a multiphase composition and presence of residual reactants.[19] Due to these limitations, in recent times, metal−organic coordination systems have been used as molecular precursors for the preparation of the mixed-metal oxides by their thermal decomposition. It has been observed that the use of a well-defined bimetallic precursor can produce crystalline oxide materials under conditions that are significantly milder than those applied in traditional solid-state synthesis. Also, the single-source precursors provide better control over the stoichiometry of the metal ions in the final products as well as the homogeneity of the materials due to the mixing of the metals at the molecular level. Further, the existence of bridging or chelating ligands in the precursors prevents metal separation during oxide formation.[19−21] An effective molecular precursor-to-material conversion requires a reasonable choice of ligands. One of the suitable ligands for the synthesis of molecular precursors for oxides is the oxalate dianion, $C_2O_4^{2-}$. The remarkable coordination ability of this anion is the basis of its wide use for the generation of homo- and heteropolynuclear species of various nuclearities or dimensionalities.[22] The $C_2O_4^{2-}$ group easily decomposes to gaseous CO_2 and CO at low temperatures, and hence, the oxalate-based solids can serve as a convenient source of oxides.[23] Heterometallic oxalate complexes have already been used for the preparation of mixed-metal oxides.[23−26]

Related to our recent magnetostructural studies on the oxalate-based metal complexes, we have extended the investigations to mixed-metal oxide phases that could be obtained by thermal decomposition of the novel heterometallic complexes. In our previous study, we reported the formation of the $Zn_3Nb_2O_8$ oxide phase, an important class of ceramic materials, by the thermal decomposition process of an oxalate-based compound of zinc(II) and niobium(V).[27] Furthermore, several new ionic Ni,Ta complex species containing the $[Ni(phen)_3]^{2+}$ cation (phen = 1,10-phenanthroline) and different (oxalato)tantalate(V) complex anions $[Ta(L)(C_2O_4)_3]^{n-}$ (L = $C_2O_4^{2-}$, OH^-, $OC_2H_5^-$, OCH_3^-; n = 2, 3) were successfully used as precursors for obtaining the $NiTa_2O_6$ oxide, which is used as a dielectric in modern telecommunication devices and as a photocatalyst for water splitting.[28] Also, in our recently published articles, the novel compound $\{Ba_2(H_2O)_5[NbO(C_2O_4)_3]HC_2O_4\}\cdot H_2O$ was used as a single-source precursor for preparation of the mixed $Ba_5Nb_4O_{15}$ and $Ba_4Nb_2O_9$ oxides through its thermal decomposition.[29] Three polymorphs of $Ba_4Nb_2O_9$ were isolated: α, γ, and the new δ modification having the 6*H*-perovskite structure. Particular attention was paid to the electrical properties of the obtained $Ba^{II}Nb^{V}$ oxides.[29a] For these reasons, we have chosen to extend our investigation on the reactions of the (oxalato)tantalate(V) solution and barium(II) ion—in this way, we isolated and characterized the oxalate-based complex $\{Ba_2(H_2O)_5[TaO(C_2O_4)_3]HC_2O_4\}\cdot H_2O$ (**1**) as a potential single-source molecular precursor for the formation of the $Ba^{II}Ta^{V}$ oxides. Generally, the tantalum oxalate complexes have been poorly studied. They have been investigated sporadically, and only a small number of crystal structures have been published.[28,30]

In this paper we present the synthesis, spectroscopic and thermal analyses, and crystal structure of a new heterometallic oxalate complex of tantalum(V) and barium(II) (**1**). A powder X-ray diffraction study revealed that γ-$Ba_4Ta_2O_9$ oxide was formed by thermal decomposition of **1**, indicating a direct molecular precursor-to-material pathway from the mixed-metal complex to the oxide. We focused on the optical, photocatalytic, and electrical properties of the nanocrystalline γ-$Ba_4Ta_2O_9$ oxide, since the transport properties have already been characterized.[31]

EXPERIMENTAL SECTION

Materials and Methods. The (oxalato)tantalate(V) solution was prepared by dissolving freshly precipitated $Ta_2O_5\cdot nH_2O$ in $H_2C_2O_4\cdot 2H_2O$, following the procedure described previously.[18,32,33] All other chemical reagents used in the synthesis were purchased from commercial sources and applied without further purification. The tantalum content in the solution was determined in the form of Ta_2O_5. Elemental analyses for C and H in **1** were carried out using a Perkin-Elmer Model 2400 microanalytical analyzer. Infrared spectra were recorded as KBr pellets using a Bruker Alpha-T spectrometer in the 4000−350 cm^{-1} range. Thermal analysis was performed on a Shimadzu DTG-60H analyzer, in the range from room temperature to 1300 °C, under a stream of synthetic air at a heating rate of 10 °C min^{-1}.

Synthesis of $\{Ba_2(H_2O)_5[TaO(C_2O_4)_3]HC_2O_4\}\cdot H_2O$ (1). An aqueous solution (10 mL) of $Ba(NO_3)_2$ (0.261 g; 1 mmol) was added dropwise to a mixture of an (oxalato)tantalate(V) solution (5 mL; m(Ta) = 0.09 g, 0.5 mmol) and 5 mL of water. A small amount of a white precipitate that formed was removed by filtration. The colorless sticklike single crystals of **1** that grew quickly from the clear solution were filtered off, washed with a small amount of water, and dried in air (the yield was ∼50%). Anal. Found: C, 10.23; H, 1.33. Calcd for $C_8H_{13}Ba_2TaO_{23}$: C, 10.30; H, 1.40. IR (KBr): $\tilde{\nu}$ 3618 (m), 3486 (s), 3429 (m), 2925 (w), 1753 (m), 1711 (vs), 1688 (vs), 1666 (vs), 1643 (s), 1411 (s), 1350 (sh), 1309 (w), 1262 (m), 937 (m), 915 (m), 851 (w), 804 (m), 724 (w), 558 (w), 531 (sh), 483 (m), 382 (m) cm^{-1}.

Single-Crystal X-ray Study. The X-ray data of a suitable single crystal of compound **1** were collected at room temperature by ω scans on an Oxford Diffraction Xcalibur 3 CCD diffractometer with graphite-monochromated Mo Kα radiation (λ = 0.71073 Å). Data reduction was performed with the CrysAlis PRO software package.[34] The structure was solved using SHELXS97[35] and refined with SHELXL97.[35] The model was refined using full-matrix least-squares refinement; all non-hydrogen atoms were refined anisotropically. Hydrogen atoms were located in a difference Fourier map and refined as mixed, free, and riding entities. Molecular geometry calculations were performed by PLATON,[36] and molecular graphics were prepared using VESTA.[37] The crystal data, experimental conditions, and final refinement parameters are summarized in Table 1.

Crystallographic data for the complex can be obtained free of charge via www.ccdc.cam.ac.uk/conts/retrieving.html (or from the Cambridge Crystallographic Data Centre, 12, Union Road, Cambridge CB2 1EZ, U.K., fax +44 1223 336033, or deposit@ccdc.cam.ac.uk). CCDC 931905 contains the supplementary crystallographic data for this paper.

Table 1. Crystallographic Data and Structure Refinement Details for Compound 1

empirical formula	$C_8H_{13}Ba_2TaO_{23}$
formula wt	930.80
space group	*Pnma*
a/Å	16.5494(3)
b/Å	11.6163(2)
c/Å	10.5414(2)
α/deg	90
β/deg	90
γ/deg	90
Z	4
V/Å^3	2026.51(6)
D_{calcd}/g cm^{-3}	3.057
μ/mm^{-1}	9.346
θ range/deg	4.19 − 32.5
T/K	293(2)
radiation wavelength/Å	0.71073
diffractometer type	Xcalibur 3 CCD
h, k, l ranges	$-7 < h < 24$
	$-17 < k < 16$
	$-13 < l < 15$
no. of rflns collected	10431
no. of indep rflns	3517
no. of obsd rflns ($I \geq 2\sigma$)	3299
R_{int}	0.0191
$R(F)$	0.0289
$R_w(F^2)$	0.0654
goodness of fit	1.292
H atom treatment	mixed
no. of params	202
no. of restraints	13
$\Delta\rho_{max}$, $\Delta\rho_{min}$ (e Å^{-3})	1.295, −1.562

Thermal Synthesis of the $Ba^{II}Ta^{V}$ Oxides. Finely ground crystalline powders of compound **1** were pressed into compact pellets (12 mm in diameter and 2 mm in thickness) under 10000 kg/cm^2, placed in an Al_2O_3 boat crucible, and heated in a furnace (Nabertherm, Model LHT 04/17) to a selected temperature in the range 600−1300 °C in air with a constant rate of 3 °C min^{-1}. At the selected temperature the resulting materials were held for 3 h and then cooled to room temperature with a cooling rate of 3 °C min^{-1}. Upon cooling, the heat-treated pellets were pulverized into a fine powder using an agate mortar and a pestle and analyzed by the X-ray powder diffraction. Electrical characterization was made on the selected heat-treated pellet.

Powder X-ray Structural and Microstructural Study. X-ray powder diffraction (XRD) patterns were measured in reflection mode with monochromated Cu Kα radiation (λ = 1.54179 Å) on a Philips PW1830 diffractometer. Rietveld refinement was performed by the HighScore X'pert Plus program (Panalytical) and Topas Academic. On the basis of a chosen structural model and a profile function, the program simulates the XRD patterns and compares them with experimental patterns in the least-squares comparison mode. Thus, a certain number of least-squares structural and profile parameters were refined. The diffraction profiles were described by a pseudo-Voigt function. A polynomial model was used to describe the background. During the refinement a zero shift, scale factor, half-width parameters (U, V, W), asymmetry parameters, and peak shape parameters were simultaneously refined. Structural parameters, atomic coordinates, and B_{iso} values were also refined. The microstructural data were obtained in the course of the Rietveld refinement in Topas Academic utilizing a double-Voigt approach.[38] LaB_6 powder was used as an instrumental broadening standard.

Computational Study. The computational part of this study was done using Kohn−Sham (KS) density functional theory (DFT)[39] with projector augmented wave (PAW) pseudopotentials[40] and the Perdew−Burke−Ernzerhof (PBE) functional,[41] as implemented in the VASP 5.1 software package.[42] The calculations were performed at the experimental lattice constants with a plane wave cutoff energy of 500 eV and a converged k-point density of 5 × 5 × 1 in a Monkhorst−Pack grid[43] and 350 extra empty bands to converge the optical tensor. To calculate absorption spectra, we used the frequency-dependent dielectric matrix calculation as implemented in VASP.[44] We have used the U correction[45] alongside the PBE functional with an effective $U - J$ value of 2.0 for Ta and 0 for other elements.

UV−Vis Diffuse Reflectance Spectroscopy. Diffuse reflectance spectra (UV−vis) were measured on powder samples using a PerkinElmer Lambda 650S spectrophotometer (Waltham, MA, USA) with a 150 mm integrating sphere in the 200−700 nm spectral range. A Spectralon reflection standard was used as a reference. The band gap energies (E_g) were estimated from the linear extrapolations of $[F(R)\cdot h\nu]^2$ and $[F(R)\cdot h\nu]^{1/2}$ vs $h\nu$ for the direct and indirect band gap transitions.

Photocatalytic Test. The photocatalytic degradation of a methyl orange solution on $Ba_4Ta_2O_9$ oxide was carried out in a custom-made circular photoreactor with 400 W Hg lamp (Photochemical Reactors Ltd.) in a water-cooled cell ($T \approx 12$ °C). A magnetic stirrer was placed at the bottom of the cell in order to maintain the homogeneity of the reaction mixture. The photoreactor walls were made of highly reflective Al foil in order to provide as high a luminous efficacy as possible. The reaction mixture contained 0.1 g of $Ba_4Ta_2O_9$ and 75 mL of a methyl orange solution with a concentration of 7 mg L^{-1}. Before illumination, the mixture was exposed to ultrasound for 10 s and stirred for 2 h in the dark in order to establish an adsorption−desorption equilibrium between the dye and the photocatalyst. The methyl orange concentration after such treatment was considered to be the initial concentration C_0. Each 1 h a 4 mL aliquot was taken out of the reaction mixture and centrifuged at 8800 rpm for 8 min. A blank test was carried out without the photocatalyst. The absorbance maximum of the methyl orange solutions at 464 nm was measured with a Perkin-Elmer Lambda 650s spectrophotometer.

Electrical Characterization. Electrical conductivity of the sample heat-treated at 1200 °C for 3 h was measured by impedance spectroscopy (Novocontrol Alpha-N dielectric analyzer) in the frequency range 0.01 Hz−3 MHz and in the temperature range 30−240 °C. For the electrical contact, gold electrodes 8 mm in diameter were sputtered onto both sides of the sample discs using a SC7620 Sputter Coater (Quorum Technologies). The measurement was performed during heating and subsequent cooling under a nitrogen atmosphere. The impedance spectra were analyzed by equivalent circuit modeling using the complex nonlinear least-squares fitting procedure (ZView software).

RESULTS AND DISCUSSION

Characterization of Compound 1. The new compound $\{Ba_2(H_2O)_5[TaO(C_2O_4)_3]HC_2O_4\}\cdot H_2O$ (**1**) was obtained in the form of colorless sticklike crystals from the reaction of an (oxalato)tantalate(V) solution and a barium(II) salt. The complex was characterized structurally, thermally, and spectroscopically. Because of a growing need for the Ta-containing oxide materials, this new oxalate-based complex was also tested as a precursor for the formation of $Ba^{II}Ta^{V}$ oxides through thermolytic conversion.

Molecular and Crystal Structure. The molecular structure of **1** consists of two Ba^{2+} cations, one $[TaO(C_2O_4)_3]^{3-}$ anion, and one hydrogen oxalate anion together with six water molecules. Compound **1** is isostructural with a recently reported analogous compound of niobium(V), $\{Ba_2(H_2O)_5[NbO(C_2O_4)_3]HC_2O_4\}\cdot H_2O$.[29a]

The Ba and Ta atoms and one of the three oxalate groups are located in a crystallographic mirror plane (p.p. 0.5); another oxalate anion is located in a general position (p.p. 1.0). In

dx.doi.org/10.1021/ic402276e | Inorg. Chem. 2013, 52, 14299−14308

addition, half of the hydrogen oxalate anion is also present, disordered about an inversion center (its centroid, i.e. midpoint of the C5−C5 bond, is located in the inversion center; therefore, p.p. 0.5), as well as three molecules of water—two of them being located in a general position (p.p. 1.0) and two halves in a mirror plane (p.p. 0.5).

The tantalum(V) atom has a distorted-pentagonal-bipyramidal structure, involving six O atoms from the three chelating oxalate groups and one oxo oxygen atom (Figure 1). The oxo

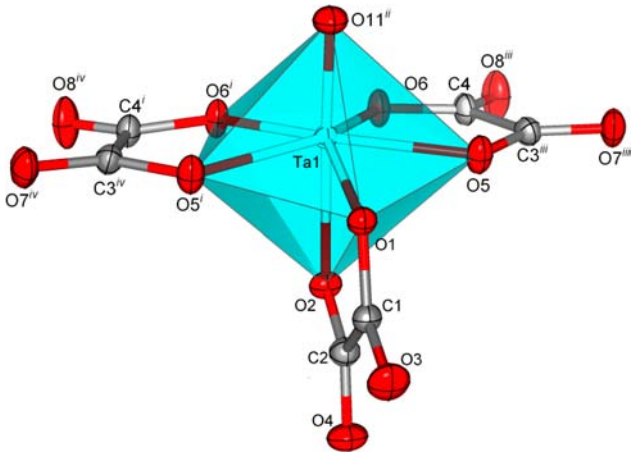

Figure 1. VESTA[37] drawing of the coordination polyhedron in the $[TaO(C_2O_4)_3]^{3-}$ anion of **1**. Displacement ellipsoids are drawn at the 50% probability level. Symmetry operators: (*i*) $x, {}^1/_2 - y, z$; (*ii*) $x, y, 1 + z$; (*iii*) ${}^1/_2 - x, -y, {}^1/_2 + z$; (*iv*) ${}^1/_2 - x, {}^1/_2 + y, {}^1/_2 + z$.

oxygen atom (O11^{ii}; symmetry operator *ii* $x, y, 1 + z$) is located in the apexes of the pentagonal bipyramid and is at the shortest interatomic distance from the Ta atom, confirming the double-bond character of the Ta═O bond (Table S1, Supporting Information). The opposite axial position of the Ta coordination polyhedron is occupied by the oxygen (O2) atom from one oxalate group. The equatorial plane of the distorted pentagonal bipyramid is defined by O1 of the same oxalate anion and O5, O6, O5^i, and O6^i (symmetry operator *i* $x, {}^1/_2 - y, z$) from the two other oxalate anions mutually related by the mirror plane (Figure 1).

Up to now, the isolation of the $[TaO(C_2O_4)_3]^{3-}$ unit has not been structurally confirmed, but there are several structurally characterized oxalate complexes in which the geometry around tantalum(V) is very similar to that in **1**.[28] In these complexes, unlike in compound **1**, the apical O atom from a monodentate group (OH^-, $OC_2H_5^-$, or OCH_3^-) is singly bonded to tantalum(V), having also three oxalate groups in the coordination sphere. The mode of coordination found in **1** is well-known in the complexes of niobium(V) when appearing in the form of the tris(oxalato)oxoniobate(V) anion, $[NbO(C_2O_4)_3]^{3-}$, in which the niobium(V) atom is doubly bonded with one oxygen atom (Nb═O).[46−48] Another interesting feature that points out the diversity of the oxalate chemistry of tantalum(V) refers to the complexes with the coordination number 8 (CN = 8; $[Ta(C_2O_4)_4]^{3-}$), as found in the recently reported species $[Hphen][Ni(phen)_3][Ta(C_2O_4)_4]\cdot 6.5H_2O$[28] and $[NH_4][(CH_3)_2NH_2]_2[Ta(C_2O_4)_4]\cdot 2H_2O$.[30] Unlike tantalum, niobium in the tetrakis(oxalato) complexes (CN = 8) appears in the +4 oxidation state (paramagnetic d^1 system), in spite of the fact that the +5 oxidation state is more favorable.[49,50]

There are two crystallographically independent Ba atoms in the crystal structure of **1**. The Ba1 atom is coordinated by 11 oxygen atoms: 6 O atoms from 4 oxalate groups, 4 O atoms from 2 hydrogen oxalate groups, and 1 O atom from a water molecule. The Ba2 atom is 10-coordinated by 4 O atoms from 3 oxalate anions, 2 O atoms from 2 hydrogen oxalate anions, O atoms from 3 water molecules, and 1 oxo oxygen atom. The coordination polyhedra around the Ba cations are shown in Figure 2, and the corresponding interatomic distances and angles are given in Tables S2 and S3 (Supporting Information).

The values of the Ba−O bond distances are in the range 2.690(5)−3.206(6) Å (average 2.922 Å; Tables S3 and S4, Supporting Information). Similarly to the compound $\{Ba_2(H_2O)_5[NbO(C_2O_4)_3]HC_2O_4\}\cdot H_2O$,[29a] Ba−O bond distances somewhat longer than the sum of covalent radii of the Ba and O atoms (2.81 Å)[51] indicate a borderline case between covalent and ionic. Therefore, compound **1** can be considered as an ionic compound or as a metal-coordinated framework.

In the crystal packing of **1**, each pentagonal-bipyramidal polyhedron of the Ta atom is linked to seven Ba polyhedra through the oxalate ligands and to one Ba polyhedron through the oxo oxygen group, whereas the Ba polyhedra share edges and vertices, as shown in Figure 3. The overall crystal arrangement is a complex 3D network, comprising a coordination framework with tantalum and barium (Figure 4). Water molecules together with oxalate groups from the $[TaO(C_2O_4)_3]^{3-}$ units are involved in a 3D hydrogen-bonding

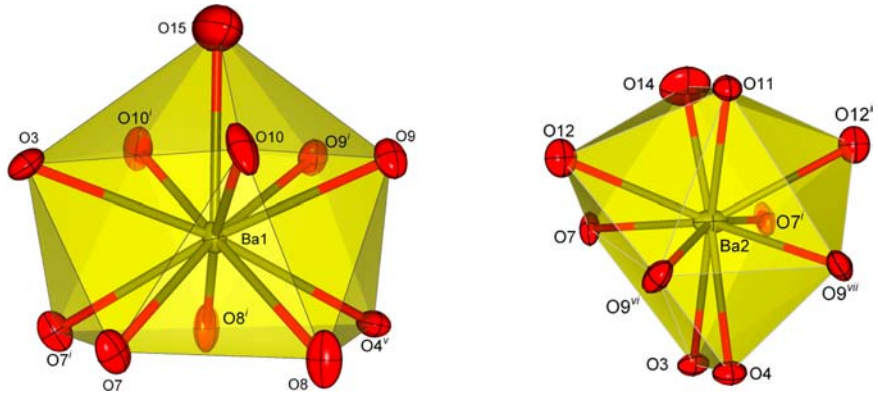

Figure 2. VESTA[37] drawing of the coordination spheres of the Ba atoms, with the atom-numbering scheme. Displacement ellipsoids are drawn at the 50% probability level. Symmetry operators: (*i*) $x, {}^1/_2 - y, z$; (*v*) ${}^1/_2 + x, {}^1/_2 - y, {}^1/_2 - z$; (*vi*) $-{}^1/_2 + x, {}^1/_2 - y, {}^1/_2 - z$; (*vii*) $-{}^1/_2 + x, y, {}^1/_2 - z$.

dx.doi.org/10.1021/ic402276e | Inorg. Chem. 2013, 52, 14299−14308

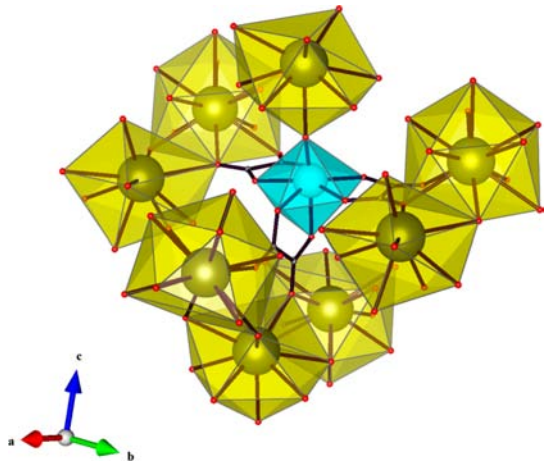

Figure 3. Pentagonal-bipyramidal polyhedron of the Ta atom linked to eight Ba polyhedra through the oxalate ligands and the oxo oxygen group, in the edge- and vertex-sharing fashion. The coordination spheres of the Ta and Ba atoms are depicted as blue and golden polyhedra, respectively.

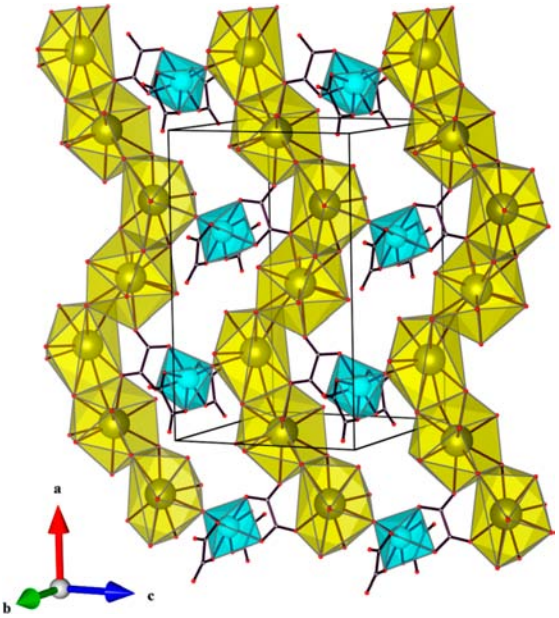

Figure 4. Packing arrangement of compound **1**, viewed in the direction [01−1]. The coordination spheres of the Ta and Ba atoms are depicted as blue and golden polyhedra, respectively.

framework. The hydrogen-bonding pattern is presented in Figure S1 (Supporting Information), and parameters are summarized in Table S4 (Supporting Information).

Thermal Study. A simultaneous TGA and DTA analysis of compound **1** was carried out under a stream of synthetic air, up to 1300 °C, and the corresponding curves are presented in Figure 5. The elimination of water molecules in **1** occurs in three successive steps that take place in the temperature interval 30−220 °C, with a few close endothermic maxima. In the first range, up to 95 °C, two water molecules are expelled (exptl 3.87%; calcd 3.86%). The second step, from 95 to 150 °C, could be associated with the removal of three molecules of the solvent (exptl 5.78%; calcd 5.79%), while the remaining molecule (exptl 2.15%; calcd 1.93%) is lost in the third step, up to 220 °C. The main loss of mass (exptl 31.18%; calcd

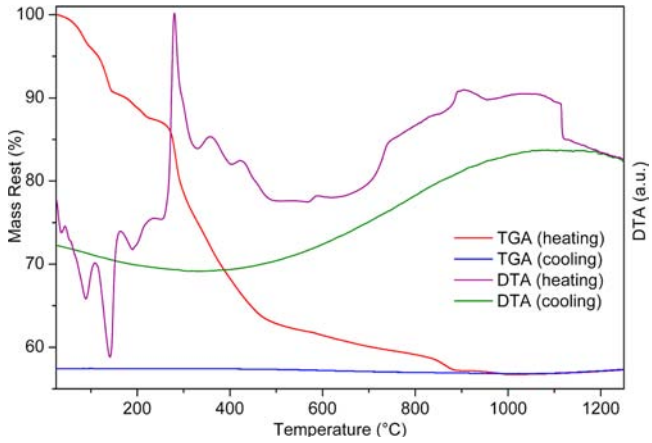

Figure 5. TGA and DTA curves (heating and cooling) for compound **1** measured under a synthetic air atmosphere.

31.85%) takes place up to 900 °C, with two steps in the TGA curve. The first step (220−450 °C) comprises the removal of the oxalate and hydrogen oxalate groups, as $2CO_2 + 4CO + {}^1/_2H_2O$ (exptl 23.74%; calcd 23.41%), followed by relatively strong exothermic DTA maxima. The loss of the remaining $2CO_2$ (probably from $2BaCO_3$) happens in the next step from 450 to 900 °C. Afterward, the mass remains almost constant. The final white residue was identified to be $Ba_4Ta_2O_9$ oxide (exptl 57.02%; calcd 56.56%). An endothermic maximum at 1118 °C in the DTA curve indicates the α-$Ba_4Ta_2O_9 \rightarrow \gamma$-$Ba_4Ta_2O_9$ phase transition, as found in the literature.[31] Furthermore, during the cooling, no maximum was noted at ∼600 °C in the DTA curve, implying that there is no reduction of the symmetry of the obtained phase (from the hexagonal $P6_3/m$ to the monoclinic $P2_1/c$ space group), as opposed to what the Ling group observed.[31]

Infrared Study. The IR spectrum of complex **1** is in agreement with the result of the X-ray analysis; the presence of chelating oxalate groups, oxo oxygen atom, and water molecules is confirmed. The broad band of medium intensity with a maximum around 3500 cm^{-1} can be assigned to the O−H stretching vibration (ν(OH)) of water molecules and hydrogen oxalate anion. The absorption bands corresponding to the oxalate groups are located at 1711, 1688, 1666, and 1643 cm^{-1} (ν_{as}(CO)), 1411, 1262, and 915 cm^{-1} (ν_s(CO)), and 804 cm^{-1} (δ(OCO)).[29a,52] The absorption bands of medium intensity present in the spectrum at 937 and 558 cm^{-1} originate from ν(Ta═O) and ν(Ta−O), respectively.[28,47]

Characterization of the γ-$Ba_4Ta_2O_9$ Phase. X-ray diffraction studies have demonstrated that the heating of precursor **1** for 3 h at 1200 °C, followed by a slow cooling to room temperature, led to formation of the hexagonal polymorph of the $Ba_4Ta_2O_9$ oxide, γ-$Ba_4Ta_2O_9$. No additional phases were found in the resulting sample, indicating the possibility that the existence of the chelating ligands in **1** prevented metal separation during the oxide formation.[19−21] Other products formed at different temperatures (in the range 750−1100 °C) contained α-$Ba_4Ta_2O_9$ as the major crystalline oxide phase. The overall molar ratio Ba:Ta in the produced γ-$Ba_4Ta_2O_9$ phase agrees well with the ratio Ba:Ta = 2:1 in the starting oxalate-based complex, confirming the efficiency of the proposed synthetic route. The γ-$Ba_4Ta_2O_9$ phase at room temperature was found to crystallize in the $P6_3/m$ space group with the unit-cell parameters a = 6.0897(1) Å and c =

dx.doi.org/10.1021/ic402276e | *Inorg. Chem.* 2013, 52, 14299−14308

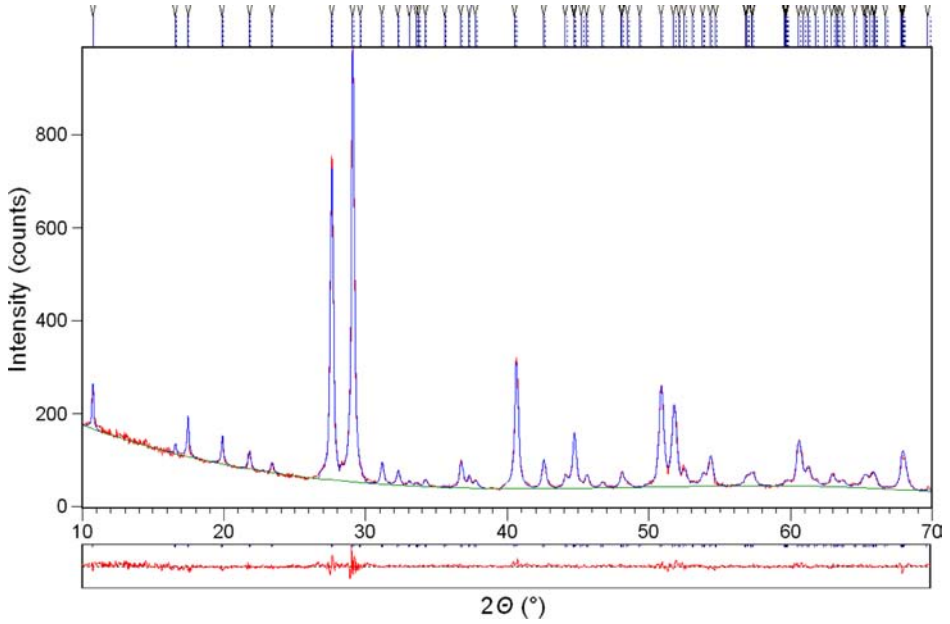

Figure 6. Graphical result of the final Rietveld refinement on the room-temperature data for γ-$Ba_4Ta_2O_9$, obtained by heat treatment of **1** at 1200 °C for 3 h, followed by cooling to room temperature. The dark blue vertical marks represent positions of the hexagonal γ-$Ba_4Ta_2O_9$ phase. Experimental data are shown in blue, the calculated pattern is shown in red, and the difference curve is given below.

16.1310(7) Å, slightly different from those reported by Ling et al.[31] The first attempt to refine the X-ray data of the product obtained by thermal treatment of **1** at 1200 °C was made in the monoclinic $P2_1/c$ space group with the unit cell parameters $a_{mon} \approx a_{hex}$, $b_{mon} \approx c_{hex}$, $c_{mon} \approx 2a_{hex}$, as suggested by Ling et al.[31] They found that even quenching below 1127 °C to room temperature led to the phase transformation of γ-$Ba_4Ta_2O_9$, from the high-temperature hexagonal ($P6_3/m$) to the monoclinic ($P2_1/c$) γ-$Ba_4Ta_2O_9$ modification stable at room temperature. This phase transition caused by the reduction of symmetry occurs at ~627 °C.[31] However, we found the lack of this transition (there is no maximum in the DTA curve during the cooling; Figure 5), resulting in the retention of the high-temperature hexagonal phase at room temperature. A plausible explanation for the retention of the high-symmetry phase at room temperature might be that particles of the high-temperature phase below a critical size do not transform to low-temperature forms, while particles above this critical size are subjected to transformation into the low-temperature phases. A similar effect of size-dependent phase transformation was observed in the case of stabilization of the high-temperature tetragonal ZrO_2 phase at room temperature.[53,54] The graphical result of the final Rietveld refinement on the laboratory powder X-ray diffraction data is shown in Figure 6; good agreement of the observed and calculated patterns unambiguously confirms the formation of the hexagonal γ-$Ba_4Tb_2O_9$ phase.

The crystal structure of the hexagonal γ-$Ba_4Ta_2O_9$ form is shown in Figure 7. Fractional atomic coordinates and thermal parameters are given in Table 2, whereas the crystal data and a summary of the structure refinement are presented in Table 3. The γ-$Ba_4Ta_2O_9$ polymorph belongs to the 6*H*-perovskite structure type, which crystallizes in the reduced-symmetry space group $P6_3/m$ and is isostructural with the low-temperature polymorph δ-$Ba_4Nb_2O_9$, which was reported recently.[29a] The structure involves distorted Ta_2O_9 face-sharing octahedral dimers aligned parallel to the *c* axis and

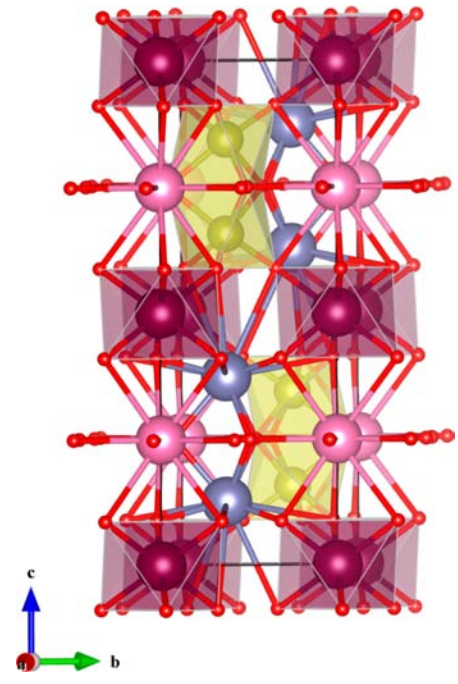

Figure 7. Crystal structure of the γ-$Ba_4Ta_2O_9$ phase. The polyhedron around the Ta atom is given in yellow. The coordination sphere of the Ba3 atom is depicted as a discrete purple octahedron. The dodecahedra around the Ba1 and Ba2 atoms are omitted for clarity.

interconnected via corners to the BaO_6 octahedra. There are two additional crystallographically different Ba atoms in the asymmetric unit. The Ba1 atom is coordinated by three O2 atoms in two adjacent layers and two groups of three O1 atoms in the same layer, achieving the coordination number 12. The Ba2 atoms are surrounded by three O1 atoms in an adjacent layer, by two groups of three O2 atoms in the same layer, and by three O2 atoms in the other adjacent layer. Selected bond distances and angles for γ-$Ba_4Ta_2O_9$ are given in Table 4.

dx.doi.org/10.1021/ic402276e | *Inorg. Chem.* 2013, 52, 14299−14308

Table 2. Fractional Atomic Coordinates and Thermal Parameters for γ-$Ba_4Ta_2O_9$

atom	Wyckoff	x	y	z	B_{iso}/Å^3
Ba1	2a	0.0000	0.0000	0.2500	0.71(2)
Ba2	4f	0.3333	0.6667	0.626(5)	0.46(4)
Ba3	2b	0.0000	0.0000	0.0000	0.55(1)
Ta	4f	0.3333	0.6667	0.1563(5)	0.91(4)
O1	6h	−0.0204(1)	0.5026(4)	0.2500	0.86(7)
O2	12i	0.3124(5)	0.38(7)	0.0889(4)	0.9(1)

Table 3. Crystal Data and Summary of Structure Refinement for γ-$Ba_4Ta_2O_9$

phase	γ-$Ba_4Ta_2O_9$
formula sum	$Ba_{8.00}Ta_{4.00}O_{18.00}$
formula mass/g mol^{-1}	1758.255
density (calcd)/g cm^{-3}	6.5436
space group (No.)	$P6_3/m$ (176)
lattice params	
a/Å	6.0897(1)
c/Å	16.1310(7)
$V/10^6$ pm^3	518.064418
fitting mode	structure fit
profile function	pseudo-Voigt
U	0.4(1)
V	0.28(4)
W	0.077(1)
asymmetry param 1	0.01(3)
peak shape param 1	0.78(1)
peak shape param 2	−0.041(3)
R(weighted profile)/%	5.4548
R(profile)/%	4.1071
GOF	1.4604

Table 4. Selected Bond Distances (Å) and Angle (deg) for γ-$Ba_4Ta_2O_9$

Bond Distances	
Ta1−O1 × 3	2.561(4)
Ta1−O2 × 3	2.407(8)
Ba3−O2 × 6	2.011(9)
Bond Angle	
O2−Ta−O1	156.7(4)

A line broadening analysis in the course of Rietveld refinement was undertaken in order to extract microstructural information concerning γ-$Ba_4Ta_2O_9$ from the XRD patterns. According to the previously established ways of tuning the crystallite size of oxide materials prepared via the thermal decomposition method,[29b] γ-$Ba_4Ta_2O_9$ was successfully prepared in the nano regime and can be characterized as a strain-free phase. The calculated maximum average lattice strain was e = 0.004(3)%; thus, it can be considered negligible. The volume-weighted domain length $\langle L_V \rangle$ for γ-$Ba_4Ta_2O_9$ amounts to 27(4) nm.

Infrared Study. Generally, metal oxides exhibit absorption bands below 1000 cm^{-1}, caused by interatomic vibrations. The infrared spectrum of the γ-$Ba_4Ta_2O_9$ phase shows two very strong absorption bands, centered at 644 and 552 cm^{-1}, that could be assigned to the asymmetric stretching mode of the metal−oxygen bond (ν_{as}(TaO)), in the Ta_2O_9 face-sharing octahedral dimer. A band of medium intensity at 771 cm^{-1} originates from the symmetric stretching vibration (ν_s(TaO)) of the same bond. The other absorption bands in the spectrum present at lower wavenumbers (482, 438, and 373 cm^{-1}) correspond to the bending vibrations (δ(OTaO)).[55] The bands associated with the Ba motions are located in the far-infrared region.

Electronic Structure and Optical Properties. The emission spectrum of the γ-$Ba_4Ta_2O_9$ phase was recorded at room temperature and is available in the Supporting Information (Figure S2). At an excitation irradiation of 405 nm, the γ-$Ba_4Ta_2O_9$ modification shows luminescence with a maximum at 546 nm. The absorption curve for γ-$Ba_4Ta_2O_9$ was calculated using the frequency-dependent dielectric matrix calculation as implemented in VASP[44] (Figure S3, Supporting Information).

The Kubelka−Munk diffuse reflectance absorption spectrum of γ-$Ba_4Ta_2O_9$ is shown in Figure 8a. γ-$Ba_4Ta_2O_9$ exhibits an absorption edge at around 260 nm. On the basis of the significantly better fit of the Kubelka−Munk plots for the direct band gap, we can assume direct band gap excitation with E_g = 5.05 eV (Figure 8b).

The band structure of the material is given in Figure 9, for the high-symmetry directions of the Brillouin zone. The K−S band gap value is 3.7 eV. It is well-known that the K−S gap is usually lower than the experimental value (Figure 8). We have also used the relatively new delta-sol method,[56] from which we obtained the bandgap value of 4.54 eV, which is in better agreement with the experimental value (Figure 8).

From the atom projected density of states given in Figure 10 the structures of the conduction band minimum (CBM) and the valence band maximum (VBM) are obtained. The valence band is mostly dominated by the oxygen p bands while the conduction bands are mostly of the d band origin of the Ba and Ta atoms.

Photocatalytic Properties. The motivation for testing the 6*H*-perovskite type γ-$Ba_4Ta_2O_9$ oxide for photocatalytic activity was found in the similarity of its crystal structures with the structures of other perovskite tantalates that show high photochemical and photocatalytic activities.[57] Even though the energy band gap of the γ-$Ba_4Ta_2O_9$ phase (E_g(calcd) = 4.54 eV; E_g(exptl) = 5.05 eV) is quite large for light absorption,[2] we have assumed that factors such as charge separation, mobility, lifetime of photogenerated electrons and holes, surface area, and active reaction sites could be more pronounced in affecting the catalytic activity, because of the nanostructure and fine crystallinity of the prepared oxide.[4,58]

The photocatalytic activity of the γ-$Ba_4Ta_2O_9$ phase was studied for the photodegradation of methyl orange under UV irradiation (frequency range from 200 to 450 nm, which excites electrons over E_g values below 6.2 eV). Figure 11 shows the degradation curves. Under applied UV light the γ-$Ba_4Ta_2O_9$ sample was found to be photocatalytically almost inactive. The decrease in methyl orange concentration before UV irradiation is due to adsorption of the dye on the photocatalyst surface. In addition to its very large band gap energy, there are also structural reasons that could explain the low photocatalytic activity. The value of the nonlinear O−Ta−O bond angle (156.7(4)°; Table 4) in γ-$Ba_4Ta_2O_9$ deviates from the value of an ideal perovskite structure (180°). Because of this, the excitation energy is less delocalized, causing the reduced movement of the photogenerated electron−hole pairs.[4,58]

Electrical Characterization. The γ-$Ba_4Ta_2O_9$ phase prepared by thermal decomposition of compound **1** (that was heated at 1200 °C for 3 h) was studied by impedance spectroscopy, and the data were analyzed by equivalent circuit modeling. Complex

dx.doi.org/10.1021/ic402276e | Inorg. Chem. 2013, 52, 14299−14308

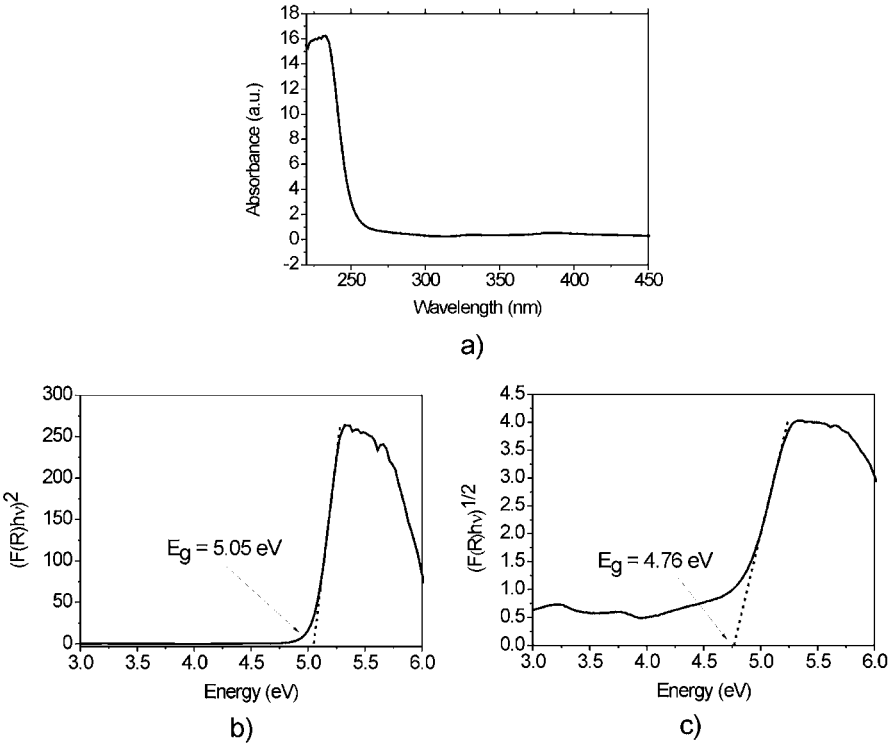

Figure 8. (a) Kubelka–Munk diffuse reflectance absorption spectra and plots for (b) direct and (c) indirect band gap evaluation of the γ-$Ba_4Ta_2O_9$ phase.

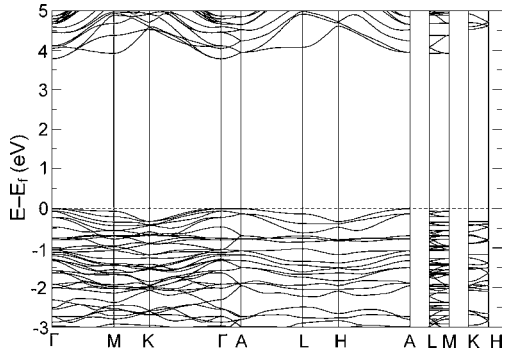

Figure 9. The calculated bandstructure of the γ-$Ba_4Ta_2O_9$ phase (space group $P6_3/m$, No. 176) for the high-symmetry directions of the Brillouin zone.

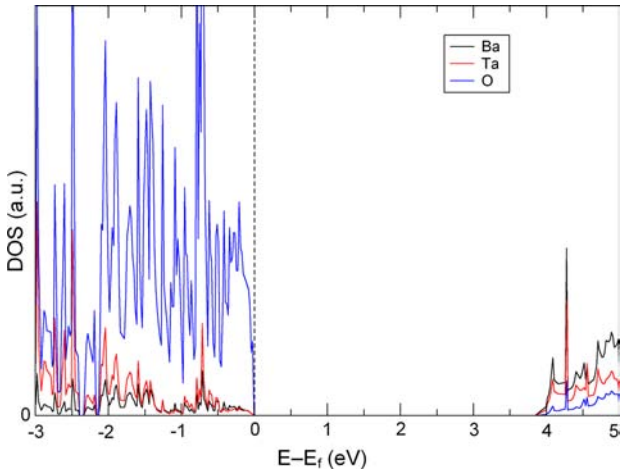

Figure 10. Atoms projected density of states of the 6*H*-perovskite type γ-$Ba_4Ta_2O_9$ (space group $P6_3/m$, No. 176).

impedance plots exhibit a single semicircle with the center below the real axis, which can be approximated by the equivalent circuit consisting of a resistor (R) and a constant-phase element (CPE) in parallel (Figure 12).

From the values of resistance, R, and the electrode dimensions (A is the electrode area and d is the sample thickness) the DC conductivity of the sample, σ_{DC}, was calculated according to the relation $\sigma_{DC} = d/(A \cdot R)$. The temperature dependence of the DC conductivity is presented in an Arrhenius plot in Figure 13.

A significant difference in electrical conductivity measured during heating and subsequent cooling is directly related to a large amount of absorbed water. In the hydrated form of γ-$Ba_4Ta_2O_9$ the dominant conductivity mechanism is protonic, leading to a high electrical conductivity, whereas in the partially dehydrated sample (cooling run) the charge transport is controlled by migration of the protons and the oxide ions. This is supported by the fact that the activation energy for conductivity determined from the slope of $\log(\sigma_{DC})$ vs $1/T$ using the equation $\sigma_{DC} = \sigma_O \exp(-E_a/k_BT)$ for the partially dehydrated γ-$Ba_4Ta_2O_9$ sample equals 85.7 kJ mol^{-1}, which is a value typical for ionic (proton and oxide ion migration) conduction. On the other hand, in the hydrated form (heating run) E_a is considerably lower because of the protonic transport with relatively low migration energy.

The electrical conductivity of the partially dehydrated γ-$Ba_4Ta_2O_9$ sample is almost identical with that of the recently reported mixture of 81.5(4) wt % of γ-$Ba_4Nb_2O_9$ and 18.5(5) wt % of δ-$Ba_4Nb_2O_9$.[29a] This result is slightly different from that reported by Ling et al.,[31] where γ-$Ba_4Ta_2O_9$ has the highest conductivity among all $Ba_4Nb_2O_9$ and $Ba_4Ta_2O_9$ polymorphs

dx.doi.org/10.1021/ic402276e | *Inorg. Chem.* 2013, 52, 14299–14308

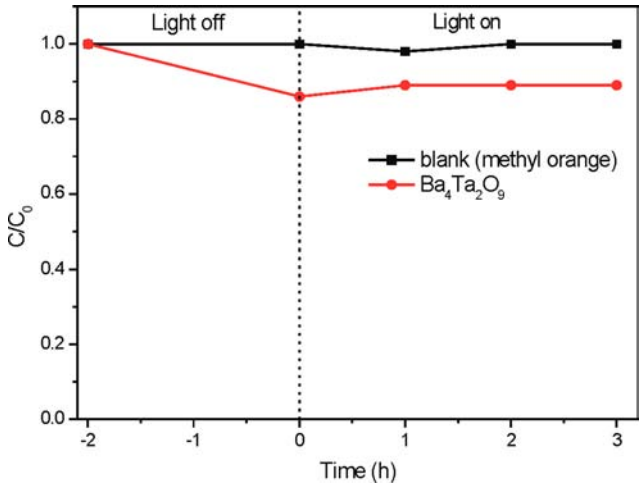

Figure 11. Temporal evolution of the absorption spectrum of methyl orange solution (7 mg L^{-1}) alone and in the presence of the γ-$Ba_4Ta_2O_9$ phase before irradiation and with UV light irradiation.

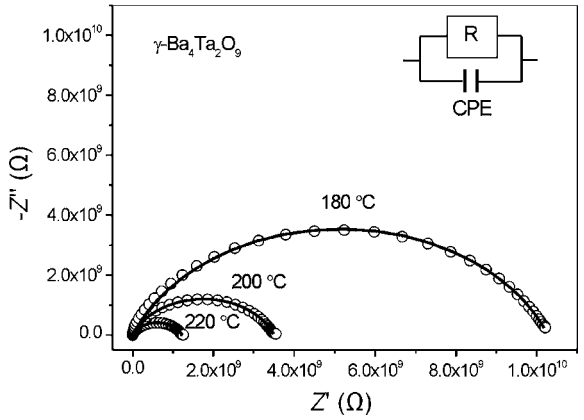

Figure 12. Complex impedance plots at 180, 200, and 220 °C and the corresponding equivalent circuits for the γ-$Ba_4Ta_2O_9$ phase. Circles denote the experimental values; solid lines correspond to the best fit.

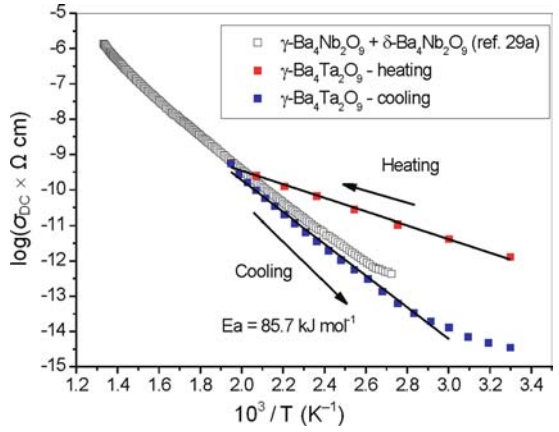

Figure 13. Temperature dependence of conductivity for the γ-$Ba_4Ta_2O_9$ phase during heating and subsequent cooling in nitrogen and the γ-$Ba_4Nb_2O_9$ + δ-$Ba_4Nb_2O_9$ mixture during cooling in nitrogen. Solid lines represent least-squares linear fits to the experimental data.

because of its unique structure with ordered proton sites. The similarity in conductivity values of the pure γ-$Ba_4Ta_2O_9$ phase and the mixture of γ-$Ba_4Nb_2O_9$ and δ-$Ba_4Nb_2O_9$ can be attributed to the structural similarities of the crystal phases γ-$Ba_4Ta_2O_9$ and δ-$Ba_4Nb_2O_9$. Moreover, all three phases exhibit high capacity for water absorption, which is essential for high proton conduction.

CONCLUSIONS

A new heterobimetallic oxalate-based complex of barium(II) and tantalum(V), $\{Ba_2(H_2O)_5[TaO(C_2O_4)_3]HC_2O_4\}\cdot H_2O$ (**1**), was prepared and characterized from a structural, thermal, and spectroscopic point of view. Thermal decomposition of this single-source precursor provided a mixed-metal oxide, the high-temperature γ-$Ba_4Ta_2O_9$ phase that is isostructural with the δ-$Ba_4Nb_2O_9$ phase that we earlier obtained as a decomposition product of $\{Ba_2(H_2O)_5[NbO(C_2O_4)_3]HC_2O_4\}\cdot H_2O$.[29] Interestingly, the reduction of symmetry $P6_3/m \rightarrow P2_1/c$ that Ling et al.[31] observed during the cooling of γ-$Ba_4Ta_2O_9$, did not occur in our samples; therefore, we retained the high-temperature γ-$Ba_4Ta_2O_9$ phase at room temperature. The band structure calculations for γ-$Ba_4Ta_2O_9$ revealed an energy gap of 4.54 eV, which support the experimentally obtained value for the direct band gap of 5.05 eV. Although it was shown that γ-$Ba_4Ta_2O_9$ is not a good photocatalyst, a large capacity for the absorption of water, reflected in the high proton conductivity, makes this phase interesting for application in the field of humidity sensors.

The new method for preparation of the γ-$Ba_4Ta_2O_9$ phase, consisting of thermal decomposition of the coordination polymer of tantalum(V) and barium(II), offers numerous benefits over the conventional ceramic method. Among them are the use of a tantalum precursor prepared from cheap and stable Ta_2O_5, low processing cost (shorter thermal treatment at lower temperature), and environmental friendliness (using only aqueous solutions).

ASSOCIATED CONTENT

Supporting Information

Figures, tables, and a CIF file giving crystallographic data for compound **1**, the full geometry of the coordination spheres of the metal atoms, a 3D hydrogen-bonding network, the geometric parameters of hydrogen bonds, the emission spectrum, the calculated absorption spectrum. This material is available free of charge via the Internet at http://pubs.acs.org.

AUTHOR INFORMATION

Corresponding Author

*M.J.: tel, +385 1 4561-189; fax, +385 1 4680-098; e-mail, Marijana.Juric@irb.hr.

Notes

The authors declare no competing financial interest.

ACKNOWLEDGMENTS

This research was supported by the Ministry of Science, Education and Sports of the Republic of Croatia (Grant Nos. 098-0982904-2946 and 098-0982929-2916) and by the Foundation of the Croatian Academy of Sciences and Arts. The authors are grateful to Dr. Marijana Đaković from the Faculty of Science, University of Zagreb, for the X-ray data collection of the single crystal of compound **1**.

REFERENCES

(1) (a) Raj, E. S; Pratt, K. F. E.; Skinner, S. J.; Parkin, I. P.; Kilner, J. A. *Chem. Mater.* **2006**, *18*, 3351−3355. (b) Wachs, I. E.; Routray, K.

ACS Catal. **2012**, *2*, 1235−1246. (c) Jung, J. H.; Lee, M.; Hong, J. I.; Ding, Y.; Chen, C. Y.; Chou, L. J.; Wang, Z. L. *ACS Nano* **2011**, *5*, 10041−10046. (d) Guo, P.; Cui, L.; Wang, Y.; Lv, M.; Wang, B.; Zhao, X. S. *Langmuir* **2013**, *29*, 8997−9003.
(2) (a) Mukherji, A.; Sun, C.; Smith, S. C.; Qing, L. G.; Wang, L. *J. Phys. Chem. C* **2011**, *115*, 15674−15678. (b) Osterloh, F. E. *Chem. Mater.* **2008**, *20*, 35−54.
(3) Zou, Z. G.; Ye, J. H.; Sayama, K.; Arakawa, H. *Nature* **2001**, *414*, 625−627.
(4) Xu, T.-G.; Zhang, C.; Shao, X.; Wu, K.; Zhu, Y.-F. *Adv. Funct. Mater.* **2006**, *16*, 1599−1607.
(5) A-Paz de Araujo, C.; Cuchiaro, J. D.; McMillan, L. D.; Scott, M. C.; Scott, J. F. *Nature* **1995**, *374*, 627−629.
(6) Xu, Y. H. *Ferroelectric Materials and Their Applications*; North Holland: Amsterdam, The Netherlands, 1991.
(7) Li, A.-D.; Kong, J.-Z.; Zhai, H.-F.; Cheng, J.-B.; Li, H.; Wu, D. *J. Am. Ceram. Soc.* **2009**, *92*, 1959−1965.
(8) Yoshino, M.; Kakihana, M.; Cho, W. S.; Kato, H.; Kudo, A. *Chem. Mater.* **2002**, *14*, 3369−3376.
(9) Calzada, M. L.; Jiménez, R.; González, A.; Mendiola, J. *Chem. Mater.* **2001**, *13*, 3−5.
(10) Calzada, M. L.; González, A.; Mendiola, J.; Jiménez, R. *Chem. Mater.* **2003**, *15*, 4775−4783.
(11) Bayot, D. A.; Devillers, M. M. *Chem. Mater.* **2004**, *16*, 5401−5407.
(12) Bayot, D.; Tinant, B.; Devillers, M. *Inorg. Chem.* **2004**, *43*, 5999−6005.
(13) Van Werde, K.; Vanhoyland, G.; Nelis, D.; Mondelaers, D.; Van Bael, M. K.; Mullens, J.; Van Poucke, L. C. *J. Mater. Chem.* **2001**, *11*, 1192−1197.
(14) Nelis, D.; Van Werde, K.; Mondelaers, D.; Vanhoyland, G.; Van Bael, M. K.; Mullens, J.; Van Poucke, L. C. *J. Eur. Ceram. Soc.* **2001**, *21*, 2047−2049.
(15) Van Bael, M. K.; Nelis, D.; Hardy, A.; Mondelaers, D.; Van Werde, K.; D'Haen, J.; Vanhoyland, G.; Van den Rul, H.; Mullens, J.; Van Poucke, L. C.; Frederix, F.; Wouters, D. J. *Integr. Ferroelectr.* **2002**, *45*, 113−122.
(16) Bouquet, V.; Longo, E.; Leite, E. R.; Varela, J. A. *J. Mater. Res.* **1999**, *14*, 3115−3121.
(17) Zanetti, S. M.; Bueno, P. R.; Leite, E.; Longo, E.; Varela, J. A. *J. Appl. Phys.* **2001**, *89*, 3416−3419.
(18) Szanics, J.; Kakihana, M. *Chem. Mater.* **1999**, *11*, 2760−2763.
(19) Bayot, D.; Tinant, B.; Devillers, M. *Inorg. Chem.* **2005**, *44*, 1554−1562.
(20) Thurston, J. H.; Whitmire, K. H. *Inorg. Chem.* **2003**, *42*, 2014−2023.
(21) Thurston, J. H.; Whitmire, K. H. *Inorg. Chem.* **2002**, *41*, 4194−4205.
(22) Allen, F. H. *Acta Crystallogr.* **2002**, *B58*, 380−388.
(23) Neo, K. E.; Ong, Y. Y.; Huynh, H. V.; Hor, T. S. A. *J. Mater. Chem.* **2007**, *17*, 1002−1006.
(24) Guo, L.; Arafune, H.; Teramae, N. *Langmuir* **2013**, *29*, 4404−4412.
(25) Rhine, W. E.; Hallock, R. B.; Davis, W. M.; Wong-Ng, W. *Chem. Mater.* **1992**, *4*, 1208−1216.
(26) Wada, S.; Narahara, M.; Hoshina, T.; Kakemoto, H.; Tsurumi, T. *J. Mater. Sci.* **2003**, *38*, 2655−2660.
(27) Jurić, M.; Planinić, P.; Brničević, N.; Matković-Čalogović, D. *J. Mol. Struct.* **2008**, *888*, 266−276.
(28) Androš, L.; Matković-Čalogović, D.; Planinić, P. *CrystEngComm* **2013**, *15*, 533−543.
(29) (a) Jurić, M.; Popović, J.; Šantić, A.; Molčanov, K.; Brničević, N.; Planinić, P. *Inorg. Chem.* **2013**, *52*, 1832−1842. (b) Popović, J.; Vrankić, M.; Jurić, M. *Cryst. Growth Des.* **2013**, *13*, 2161−2165.
(30) Perić, B.; Brničević, N.; Jurić, M.; Planinić, P.; Matković-Čalogović, D. *Struct. Chem.* **2009**, *20*, 933−941.
(31) Ling, C. D.; Avdeev, M.; Kharton, V. V.; Yaremchenko, A. A.; Macquart, R. B.; Hoelzel, M. *Chem. Mater.* **2010**, *22*, 532−540.
(32) Androš, L.; Jurić, M.; Planinić, P.; Žilić, D.; Rakvin, B.; Molčanov, K. *Polyhedron* **2010**, *29*, 1291−1298.
(33) BrauerG.*Handbuch der Präparativen Anorganischen Chemie*, 2. Aufl., 2. Band; Ferdinand Enke Verlag: Stuttgart, Germany, 1962.
(34) *CrysAlis PRO*; Oxford Diffraction Ltd., Oxford, U.K., 2007.
(35) Sheldrick, G. M. *Acta Crystallogr.* **2008**, *A64*, 112−122.
(36) Spek, A. L. *J. Appl. Crystallogr.* **2003**, *36*, 7−13.
(37) Momma, K.; Izumi, F. *J. Appl. Crystallogr.* **2011**, *44*, 1272−1276.
(38) Balzar, D. In *Defect and Microstructure Analysis from Diffraction*; Snyder, R. L., Bunge, H. J., Fiala, J., Eds.; IUCr/Oxford University Press: New York, 1999; pp 94−126.
(39) (a) Hohenberg, P.; Kohn, W. *Phys. Rev.* **1964**, *136*, B864−B871. (b) Kohn, W.; Sham, L. J. *Phys. Rev.* **1965**, *140*, A1133−A1138.
(40) (a) Blöchl, P. E. *Phys. Rev. B* **1994**, *50*, 17953−17979. (b) Kresse, G.; Joubert, D. *Phys. Rev. B* **1999**, *59*, 1758−1775.
(41) Perdew, J. P.; Burke, K.; Ernzerhof, M. *Phys. Rev. Lett.* **1996**, *77*, 3865−3868.
(42) (a) Kresse, G.; Hafner, J. *Phys. Rev. B* **1993**, *47*, 558−561. (b) Kresse, G.; Furthmüller, J. *Phys. Rev. B* **1996**, *54*, 11169−11186.
(43) Monkhorst, H. J.; Pack, J. D. *Phys. Rev. B* **1976**, *13*, 5188−5192.
(44) Gajdoš, M.; Hummer, K.; Kresse, G.; Furthmüller, J.; Bechstedt, F. *Phys. Rev. B* **2006**, *73*, 045112.
(45) (a) Anisimov, V. I.; Zaanen, J.; Andersen, O. K. *Phys. Rev. B* **1991**, *44*, 943−954. (b) Anisimov, V. I.; Solovyev, I. V.; Korotin, M. A.; Czyżyk, M. T.; Sawatzky, G. A. *Phys. Rev. B* **1993**, *48*, 16929−16934. (c) Liechtenstein, A. I.; Anisimov, V. I.; Zaanen, J. *Phys. Rev. B* **1995**, *52*, R5467−R5470. (d) Dudarev, S. L.; Botton, G. A.; Savrasov, S. Y.; Humphreys, C. J.; Sutton, A. P. *Phys. Rev. B* **1998**, *57*, 1505−1509.
(46) Jurić, M.; Perić, B.; Brničević, N.; Planinić, P.; Pajić, D.; Zadro, K.; Giester, G.; Kaitner, B. *Dalton Trans.* **2008**, 742−754.
(47) Šestan, M.; Perić, B.; Giester, G.; Planinić, P.; Brničević, N. *Struct. Chem.* **2005**, *16*, 409−414.
(48) Mathern, G.; Weiss, R. *Acta Crystallogr.* **1971**, *B27*, 1610−1618.
(49) Cotton, F. A.; Diebold, M. P.; Roth, W. J. *Inorg. Chem.* **1987**, *26*, 2889−2893.
(50) Ooi, B.-L.; Shihabara, T.; Sakane, G.; Mok, K.-F. *Inorg. Chim. Acta* **1997**, *266*, 103−107.
(51) Cordero, B.; Gómez, V.; Platero-Prats, A. E.; Revés, M.; Echeverria, J.; Cremades, E.; Barragán, F.; Alvarez, S. *Dalton Trans.* **2008**, 2832−2838.
(52) Nakamoto, K. *Infrared and Raman Spectra of Inorganic and Coordination Compounds*, 6th ed.; Wiley: New York, 2009.
(53) Garvie, R. C. *J. Phys. Chem.* **1978**, *82*, 218−224.
(54) Shukla, S.; Seal, S.; Vij, R.; Bandyopadhyay, S.; Rahman, Z. *Nano Lett.* **2002**, *2*, 989−993.
(55) Dias, A.; Bijumon, P. V.; Sebastian, M. T.; Moreira, R. L. *J. Appl. Phys.* **2005**, *98*, 084105.
(56) Chan, M. K. Y.; Ceder, G. *Phys. Rev. Lett.* **2010**, *105*, 196403.
(57) Kudo, A.; Kato, H.; Nakagawa, S. *J. Phys. Chem. B* **2000**, *104*, 571−575.
(58) Kudo, A. *Catal. Surv. Asia* **2003**, *7*, 31−38.